# Magnetic structure of the mixed antiferromagnet $NdMn_{0.8}Fe_{0.2}O_3$

Matúš Mihalik,[1,*] Marián Mihalik,[1] Andreas Hoser,[2] Daniel M. Pajerowski,[3] Dominik Kriegner,[4] Dominik Legut,[5] Kristof M. Lebecki,[5] Martin Vavra,[6] Magdalena Fitta,[7] and Mark W. Meisel[8,9,10,†]

[1]*Institute of Experimental Physics SAS, Watsonova 47, 040 01 Košice, Slovak Republic*

[2]*Helmholtz-Zentrum Berlin, Hahn-Meitner-Platz 1, 14109 Berlin, Germany*

[3]*Quantum Condensed Matter Division, Neutron Sciences Directorate, Oak Ridge National Laboratory, Oak Ridge, Tennessee 37831, USA*

[4]*Department of Condensed Matter Physics, Faculty of Mathematics and Physics, Charles University, Ke Karlovu 5, CZ-121 16 Praha 2, Czech Republic*

[5]*Nanotechnology Centre & IT4Innovations Center, VSB-Technical University of Ostrava, 17. listopadu 15, CZ-708 33 Ostrava, Czech Republic*

[6]*Department of Inorganic Chemistry, Institute of Chemistry, Faculty of Science, P. J. Šafárik University, Moyzesova 11, 041 54 Košice, Slovak Republic*

[7]*Institute of Nuclear Physics Polish Academy of Sciences, Radzikowskiego 152, 31-342 Kraków, Poland*

[8]*Department of Physics and National High Magnetic Field Laboratory, University of Florida, Gainesville, Florida 32611-8440, USA*

[9]*Joint Institute for Neutron Sciences, Oak Ridge National Laboratory, Oak Ridge, Tennessee 37831-6453, USA*

[10]*Department of Condensed Matter Physics, Institute of Physics, Faculty of Science, P. J. Šafárik University, Park Angelinum 9, 041 54 Košice, Slovak Republic*

The magnetic structure of the mixed antiferromagnet $NdMn_{0.8}Fe_{0.2}O_3$ was resolved. Neutron powder diffraction data definitively resolve the Mn sublattice with a magnetic propagation vector $\mathbf{k} = (000)$ and with the magnetic structure $(A_x, F_y, G_z)$ for $1.6\text{ K} < T < T_N (\approx 59\text{ K})$. The Nd sublattice has a $(0, f_y, 0)$ contribution in the same temperature interval. The Mn sublattice undergoes a spin-reorientation transition at $T_1 \approx 13$ K while the Nd magnetic moment abruptly increases at this temperature. Powder x-ray diffraction shows a strong magnetoelastic effect at $T_N$ but no additional structural phase transitions from 3 to 300 K. Density functional theory calculations confirm the magnetic structure of the undoped $NdMnO_3$ as part of our analysis. Taken together, these results show that the magnetic structure of the Mn sublattice in $NdMn_{0.8}Fe_{0.2}O_3$ is a combination of the Mn and Fe parent compounds, but the magnetic ordering of the Nd sublattice spans a broader temperature interval than in the case of $NdMnO_3$ and $NdFeO_3$. This result is a consequence of the fact that the Nd ions do not order independently, but via polarization from the Mn/Fe sublattice.

## I. INTRODUCTION

Complex oxides, of which manganites are a subset, host multiferroicity and magnetoelectricity [1]. One motivation for investigating $R_{1-x}A_x MnO_3$ hole-doped manganites, where $R$ is a rare earth and $A$ is an alkali-metal element, is colossal magnetoresistance (CMR) [2,3]. The most studied CMR material is $La_{1-x}Ca_x MnO_3$, which shows a complex interplay between magnetic, charge, and structural order, all of which may affect CMR [4], and the $Nd_{1-x}Ca_x MnO_3$ material shows similar CMR features [5]. Recently, neutron scattering experiments and density functional theory analysis of $SrMnO_3$ and $NdMnO_3$ heterostructures displayed an interfacial ferromagnetism that is a step toward manganite-based multiferroic devices [6].

$NdMn_{1-x}Fe_x O_3$ is a magnetic insulator that contains three ions with well-documented magnetochemistry [7]. The $Nd^{3+}$ has a $4f^3$, 10-fold degenerate magnetic $^4I$ ground state that is split and mixed in the perovskite host lattice to have both orbital and spin components. The $Mn^{3+}$ ion is $S = 2$, $3d^4$ with

a Jahn-Teller active $^5E_g$ ground state. The $Fe^{3+}$ ion has a half-full $d$-shell $S = 5/2$, $^6A_1$ ground state. An understanding of the alloyed, solid-solution materials begins with a description of the well-studied end members $NdMnO_3$ and $NdFeO_3$. In the following, the discussion will be restricted to $T > T_{Nd} \approx 1.5$ K, where the Nd-Nd interaction becomes important and an additional order parameter must be introduced [8].

Neutron diffraction studies have shown that $NdMnO_3$ is an $A$-type antiferromagnet, where the Mn sublattice orders to make it into a $\mu_{Mn} = (A_x, F_y, 0)$ [9] or $\mu_{Mn} = (A_x, 0, 0)$ [10] magnetic structure below $T_N = 82$ K [9,10]. The moment axes are dictated by the strong anisotropy ($D \approx 5$ K) of the Jahn-Teller distorted manganese [11]. In $NdMnO_3$, below $T_1 = 20$ K, there is a second transition that is associated with a ferromagnetic Mn-Nd interaction causing ordering of the Nd sublattice to the $\mu_{Nd} = (0, f_y, 0)$ magnetic structure [9,10], while no effect on the Mn sublattice was observed [9] nor was any additional canting of the Mn moments to the $\mu_{Mn} = (A_x, F_y, 0)$ reported [10]. It is noteworthy that, due to antisymmetric exchange, weak ferromagnetism in $RMnO_3$ compounds gives $(A_x, F_y, 0)$ ordering, with $F_y$ and/or $A_x$ being rather small for the majority of light rare-earth ions [9,10,12–14]. In addition, the magnetic excitation of the Nd ions below $T_1$ has been confirmed by a neutron backscattering experiment [15] with

*matmihalik@saske.sk

†meisel@phys.ufl.edu

no applied magnetic field, but the same experiment revealed nonzero polarization of the Nd ions below 40 K, while x-ray magnetic circular dichroism data acquired in an applied magnetic field showed ordering of the Nd sublattice below $T_N$ [16].

NdFeO$_3$ is a $G$-type antiferromagnet with weak ferromagnetism with $\mu_{Fe} = (0, F_y, G_z)$[1] and $T_N = 690$ K [17,18]. The Fe octahedra in NdFeO$_3$ are nearly isotropic, in contrast to NdMnO$_3$, with a much weaker magnetic anisotropy ($D < 0.1$ K). Indeed, anisotropy in orthoferrites is subtle enough that spin reorientation due to octahedra rotation as a function of temperature is typical, and in NdFeO$_3$, the iron moments undergo a continuous transition to $(0, G_y, F_z)$ from 167 to 125 K concomitant with an octahedra rotation [19]. For $T < 10$ K, the Nd-Fe interaction induces a noticeable Nd moment [8] that has a gradual onset into the $(c_x, 0, f_z)$ structure, with the difference that the spins of the two sublattices are antiparallel in NdFeO$_3$ [8,19]. Neutron backscattering has also confirmed the Nd magnetic moment in NdFeO$_3$ for temperatures below 4.5 K [20].

So in the context of the two pure end-point compounds, NdMn$_{1-x}$Fe$_x$O$_3$ is a mixed-anisotropy, mixed-type antiferromagnet with a phase diagram reported for $0 \leqslant x \leqslant 0.5$ that shows a similar suppression of $T_N$ in the given $x$ interval to other members of the $R$Mn$_{1-x}$Fe$_x$O$_3$ family [21–24]. Recently, additional investigations have been performed for $0 \leqslant x \leqslant 0.3$ [25–27]. The substitution of Fe$^{3+}$ for Mn$^{3+}$ ions modifies the superexchange interactions, alters the polarization of the Nd$^{3+}$ ions through the Nd-Mn and Nd-Fe interactions, and changes the electron-phonon coupling due to reduction of the Jahn-Teller effect [28]. Although NdFeO$_3$ has a significantly higher ordering temperature than NdMnO$_3$, $T_N$ is found to *decrease* monotonically with iron doping in the range of $0 \leqslant x \leqslant 0.3$ that was studied [25]. On the other hand, below $T_N$, a low-temperature magnetic transition, $T_1$, defined by an anomaly in the ac susceptibility decreases with increasing doping [25]. Extrapolating from the NdMnO$_3$ compound, this anomaly was tentatively assigned to the ordering of Nd ions [25], although no microscopic study of this transition has been published until now. The ac susceptibility peak width of $T_N$ broadens with increasing $x$ for both in-phase ($\chi'$) and out-of-phase ($\chi''$) components. The ac peak associated with $T_1$ varies nonmonotonically in position between 11 and 16 K and also in intensity, with the maximum intensity of $\chi'$ and $\chi''$ when $x = 0.2$. Furthermore, hysteretic behavior between magnetization measurements with zero-field-cooled (ZFC) and field-cooled (FC) protocols was observed, while magnetic pole inversion, with a compensation temperature near 27 K, was observed for samples with $x = 0.2$ and 0.25 [25].

The alloying of different types of antiferromagnets has previously been studied in detail to understand the oblique antiferromagnetic (OAF) phase where spins point at an angle between those of the parent compounds, and three classic examples are the highly two-dimensional Fe$_{1-x}$Co$_x$Cl$_2$ [29] and the three-dimensional, hexagonal K$_2$Mn$_{1-x}$Fe$_x$F$_4$ [30] and Fe$_x$Co$_{1-x}$TiO$_3$ [31] compounds. Such compounds show the characteristic dip in ordering temperatures between the two

parent compounds with a minimum at a tricritical point in the $x$-$T$ plane, similar to the $R$Mn$_{1-x}$Fe$_x$O$_3$ family of compounds [21–24]. In addition, the CMR material Ca$_{1-x}$Sm$_x$MnO$_3$ is a pseudoperovskite manganite that showed phase separation into $C$-type and $G$-type antiferromagnetism [32]. Given the different magnetic behavior above and below $x = 0.2$ for NdMn$_{1-x}$Fe$_x$O$_3$, the present neutron powder diffraction (NPD) work was undertaken to determine the magnetic structure of the mixed $A$-type and $G$-type magnetism on a three-dimensional cubic lattice NdMn$_{0.8}$Fe$_{0.2}$O$_3$, which is near the OAF phase approaching the tricritical doping.

Herein, our NPD data establish that NdMn$_{0.8}$Fe$_{0.2}$O$_3$ orders magnetically with a magnetic propagation vector $\mathbf{k} = (000)$. The $3d$ ions order into $(A_x, F_y, G_z)$ magnetic structure and Nd$^{3+}$ ions order into $(0, f_y, 0)$ magnetic structure in the interval $1.6$ K $< T < T_N$ ($\approx 59$ K); see Fig. 1. At $T_1 \approx 13$ K, a spin reorientation transition was observed, and this change is likely the origin of the anomalies reported from bulk measurements [25]. The details of moment assignment will be discussed in the context of experimental and theoretical work, and the presentation begins with the synthesis and experimental protocols presented in Sec. II. In Sec. III, results from temperature-dependent x-ray powder diffraction (XRPD) data are presented and have been used to study the structural properties of the sample, while NPD has been used to extract the magnetic structure. Section IV describes the energies from density functional theory (DFT) of the four most probable magnetic structures in the numerically tractable *undoped* NdMnO$_3$. Finally, a coherent picture of these results is discussed in Sec. V and summarized in Sec. VI.

## II. EXPERIMENTAL METHODS, ANALYSIS PROTOCOLS, AND COMPUTATIONAL DETAILS

### A. Sample preparation and characterization

Samples were prepared by a vertical floating zone (FZ) method in an optical mirror furnace. The starting materials consisted of high-purity oxides of MnO$_2$ (purity 3N, Alpha Aesar), Nd$_2$O$_3$ (purity 3N, Sigma Aldrich), and Fe$_2$O$_3$ (purity 2N, Sigma Aldrich). These starting materials were mixed in a stoichiometric ratio, isostatically cold-pressed into rods, and subsequently sintered at $1100\,^\circ$C for 12–24 h in air. The sintering procedure followed the solid-state reaction preparation route [35], and the starting rods were already partially recrystallized after heat treatment. The floating zone experiment was performed using a four-mirror optical furnace equipped with 1 kW halogen lamps and a pulling speed of 6 mm/h, a feeding speed of 4 mm/h, and a flowing (2 $\ell$/min) air atmosphere. The oxygen content was checked by iodometric titration, where a known amount of sample was dissolved in HCl solution (1:1, v/v) in the presence of KI. Immediately, the color of the solution turned to yellow from I$_2$ arising from the oxidation of iodine anions. Simultaneously with iodine oxidation, the manganese reduction proceeds to the 2+ oxidation state. Finally, after completely dissolving the sample, the amount of iodine was determined by iodometric titration with Na$_2$S$_2$O$_3$ solution. Ultimately, a small excess of oxygen was detected, amounting to $\delta = 0.065$ for NdMn$_{0.8}$Fe$_{0.2}$O$_{3+\delta}$, and this excess oxygen indicates that trace

---

[1]Unless otherwise stated, the data and analysis reported herein use the orthorhombic space group *Pnma*.
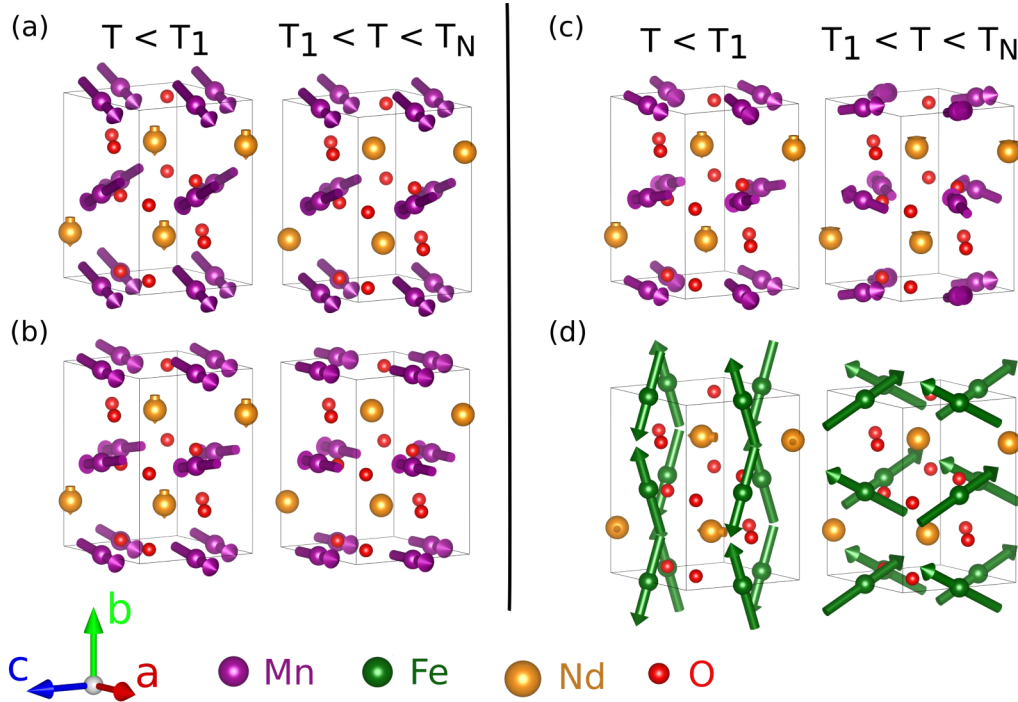
FIG. 1. Determined magnetic structures for (a) $NdMnO_3$ ($T_1 \approx 13$ K; $T_N \approx 78$ K) by Muñoz *et al.* [9]; (b) $NdMnO_3$ ($T_1 \approx 20$ K; $T_N \approx 82$ K) by Chatterji *et al.* [10]; (c) $NdMn_{0.8}Fe_{0.2}O_3$ ($T_1 \approx 13$ K; $T_N \approx 59$ K), this work; and (d) $NdFeO_3$ (left panel: $T < 10$ K; right panel: $T_1 \approx 167$ K; $T_N = 690$ K) from other authors [8,19,20]. The additional 2D projections of the magnetic structures are presented in Fig. SM1 of Supplemental Material (SM) [33]. This drawing was made using the program VESTA [34].

amounts of $Mn^{4+}$ ions are incorporated in our sample, which we will refer to as $NdMn_{0.8}Fe_{0.2}O_3$.

It is generally accepted that solid solutions with a uniform chemical composition can be prepared by FZ techniques. To verify this assumption, the crystal structure of $NdMn_{0.8}Fe_{0.2}O_3$ was investigated by x-ray powder diffraction (XRPD), and all of the samples were established to be single-phase. Next, two parts of the sample, one from the start and one from the end of the resulting ingot, were investigated by a scanning electron microscope (SEM), Mira III FE (produced by Tescan), which was equipped with an energy-dispersive x-ray (EDX) analyzer, PentaFET Precision (produced by Oxford Instruments). The SEM and EDX investigations revealed that both parts of the ingot were free of any inclusions, and no concentration gradient between the two ends of the crystal was detected. Finally, the Nd:Mn:Fe ratio of 1:0.8:0.2, as determined by EDX analysis, was consistent with the other determinations within experimental uncertainties.

### B. Neutron diffraction studies

The initial neutron powder diffraction (NPD) experiment was performed on the E6 neutron powder diffractometer at the Helmholtz-Zentrum Berlin (HZB). A freshly ground powder sample with mass of about 5 g was enclosed, along with He exchange gas, in a vanadium container with a diameter of 5 mm. The settings of the diffractometer were as follows (downstream from the nuclear reactor): 30′ Soller slit, pyrolytic graphite (PG) monochromator ($\lambda = 0.2454$ nm), PG filter, 30′ Soller slit, sample enclosed in standard Orange cryostat, moving fan collimator, two position-sensitive detectors. Long

scans were collected for $12.7° < 2\theta < 102°$ at temperatures of 1.6, 20, 35, and 65 K. In addition, several short scans ($12° < 2\theta < 66°$) were acquired in the temperature range $1.6 < T < 65$ K.

An additional NPD experiment was performed on HB-3 triple-axis neutron spectrometer at the High Flux Isotope Reactor (HFIR) located at Oak Ridge National Laboratory (ORNL). During the experiment, the spectrometer was configured for elastic scattering with incident neutron energy 14.7 meV and $\lambda = 0.236$ nm. Soller collimations of reactor $− 48′ −$ mono $−40′ −$ sample $− 40′ −$ analyzer $− 240′ −$ detector were used, with slits optimized at a Bragg peak. For this experiment, approximately 20 g of freshly ground powder along with He exchange gas was confined to an aluminum sample can, which was attached to a standard insert used with a standard Orange cryostat. The one-day experiment focused on collecting data for $28° \leqslant 2\theta \leqslant 33°$ at temperatures of 1.7, 20, and 65 K.

### C. Low-temperature XRPD studies

Low-temperature XRPD was performed using a refurbished Siemens D500 diffractometer equipped with a closed-cycle cryocooler (Sumitomo Heavy Industries) enabling measurements over a range of temperatures ($3 \leqslant T \leqslant 300$ K). Data were acquired with Cu $K_{\alpha1,2}$ radiation and a Bragg-Brentano geometry with a source-sample and sample-detector distance of 330 mm. The sample environment consisted of a single crystalline sapphire sample holder, providing good thermal equilibration and low diffraction background, and He exchange gas to ensure homogeneous sample temperature. The measurements were performed in reflection geometry with a

fixed divergence slit size, resulting in a primary beam with $0.44°$ divergence. A linear detector (MYTHEN 1 K) along with an optimized integration procedure [36] were used to avoid geometrical defocusing, while a Ni foil was used to remove the $K_\beta$ radiation.

### D. Diffraction analysis protocols and programs

All diffraction data were fitted using Le Bail and Rietveld methods implemented in the FULLPROF program [37]. The background was modeled by a polynomial function of maximum fifth order for room temperature (RT) XRPD data and NPD data. The background for the low-temperature (LT) XRPD data was estimated manually due to a nontrivial shape caused by scattering by the windows of the sample chamber. Since the instrumental functions of the apparatuses were not established, the peak shape was modeled by a Thompson-Cox-Hastings pseudo-Voigt function for the XRPD and by a Gaussian function for the NPD data. The initial conjectures of the profile functions for the NPD and LT XRPD data sets were obtained by Le Bail fits of a YIG standard and a $LaB_6$ NIST standard (standard number 660b), respectively. For describing the magnetic contributions to the NPD data, the standard magnetic form factors for $Mn^{3+}$, $Fe^{3+}$, and $Nd^{3+}$ ions that are incorporated in the FULLPROF program [37] were used. All parameters allowed by the crystal symmetry of the crystallographic unit cell were refined. The symmetry analysis was performed using the program BASIREPS, which is part of the FULLPROF suite package of programs [38]. To find the global minimum of the best magnetic model, we have generated large seeds of starting magnetic moments by a home-written java program. In these seeds, $\mu_{Mnx}$, $\mu_{Mny}$, and $\mu_{Mnz}$ starting values were tabulated in the interval $-4 \mu_B$ to $4 \mu_B$; $\mu_{Fex}$, $\mu_{Fey}$, and $\mu_{Fez}$ starting values in the interval $-5 \mu_B$ to $5 \mu_B$; and the $\mu_{Ndy}$ starting value was in the interval $0-3.2 \mu_B$ with steps between $0.5 \mu_B$ and $1.5 \mu_B$, depending on the complexity of the calculations. Each point from this starting seed was then loaded separately into the FULLPROF program and refined for 10 cycles to get the representative values of the $R$ factors.

### E. Computational details

The first-principles (*ab initio*) calculations are based on the density functional theory [39] within the single-electron framework and are used herein to treat the pure stoichiometric $NdMnO_3$ compound. The VASP (Vienna *Ab-initio* Simulation Package) package [40,41], a plane-wave pseudopotential code, was used to perform spin-polarized calculations including the spin-orbit interaction. Projector-augmented-wave pseudopotentials were used for Nd, Mn, and O atoms with the electronic valence configurations of [Xe] $4f^3$ (oxidation state $3^+$), [Ar] $3d^5 4s^2$, and [He] $2s^2 2^4$, respectively. General gradient-corrected exchange-correlation functionals parametrized by Perdew-Burke-Ernzerhof (PBE) [42] and a plane-wave cutoff of 600 eV were employed. The unit cell was sampled with a $k$-point mesh of $6 \times 4 \times 6$ generated according to the scheme proposed by Monkhorst and Pack [43]. The convergence criteria for the total energies and forces were set to $10^{-6}$ eV and $10^{-4}$ eV/Å, respectively. Electron correlation beyond the PBE

was taken into account within the framework of the so-called GGA+U method and the approach proposed by Dudarev *et al.* [44]. Calculations were carried out with the Coulomb repulsion $U$ and the exchange parameter $J$ in the range of 0.1–10 eV for the $d$ and $f$ electrons of Mn and Nd atoms. The spin-orbit interaction of the valence states was taken into account.

## III. RESULTS

### A. Crystal structure refinement

The crystal structure of $NdMn_{0.8}Fe_{0.2}O_3$ was refined from the XRPD and NPD data at room temperature. The process was performed by first treating the XRPD and the NPD data sets separately. Subsequently, these two diffractograms were co-refined, but due to the different measuring statistics, as evidenced by the resolution of the (110) peak, the XRPD to NPD data were weighted 0.6 to 0.4. Since $NdMnO_3$ and $NdFeO_3$ adopt the same crystal structure [9,19] (orthorhombic structure, space group $Pnma$, with atomic positions Mn/Fe: $4b$; Nd: $4c$; $O_1$: $4c$; $O_2$: $8d$), the crystal structure of $NdMnO_3$ reported by Muñoz *et al.* [9] was used as a starting model. The Rietveld fit using this model resulted in low $R$-factors, and it led to the crystallographic parameters presented in Table I, and these results indicate that $NdMn_{0.8}Fe_{0.2}O_3$ maintains the structure of the parent compound $NdMnO_3$. To determine the rare-earth deficiency [45], the occupancy factor of the Nd atoms was allowed to vary during the first stages of the refinement of the NPD data, and the value converged to 1.04(1), thereby indicating no appreciable evidence of Nd nonstoichiometry. Consequently, the Nd site was considered to be fully occupied in the next stages of refinement and for the processing of all experimental data collected below room temperature.

The calculated lattice parameters decrease monotonically in the temperature range $80 \leqslant T \leqslant 300$ K (Fig. 2), and the observed changes are consistent with thermal contraction. Below 65(10) K, there is a clear increase of the $c$-axis length, while the $a$-axis, $b$-axis, and volume changes are more subtle.

TABLE I. Comparison of the crystallographic parameters of $NdMn_{0.8}Fe_{0.2}O_3$ as obtained from the different diffraction techniques at room temperature. The resulting $R$ factors are as follows: $R_p = 20.0$, $R_{wp} = 25.8$, $R_{exp} = 14.3$, and $\chi^2 = 3.24$ for XRPD data; $R_p = 4.81$, $R_{wp} = 6.73$, $R_{exp} = 4.23$, and $\chi^2 = 2.53$ for NPD data; and $R_p = 20.5$, $R_{wp} = 19.8$, $R_{exp} = 1.97$, and $\chi^2 = 3.80$ for the co-refined fit described in the text.

|  | XRPD | NPD | Co-refined fit |
|---|---|---|---|
| $a$ (nm) | 0.5772(2) | 0.5781(4) | 0.5772(2) |
| $b$ (nm) | 0.7600(3) | 0.7630(6) | 0.7603(3) |
| $c$ (nm) | 0.5419(2) | 0.5439(4) | 0.5422(2) |
| $V$ (nm$^3$) | 0.2377(2) | 0.2399(3) | 0.2379(4) |
| $x_{Nd}$ | 0.065(2) | 0.064(6) | 0.059(5) |
| $z_{Nd}$ | 0.984(3) | 0.973(1) | 0.977(4) |
| $x_{O1}$ | 0.487(9) | 0.478(3) | 0.481(3) |
| $z_{O1}$ | 0.081(8) | 0.087(9) | 0.096(5) |
| $x_{O2}$ | 0.326(7) | 0.315(5) | 0.316(4) |
| $y_{O2}$ | 0.038(7) | 0.040(6) | 0.028(7) |
| $z_{O2}$ | 0.705(7) | 0.708(6) | 0.705(4) |
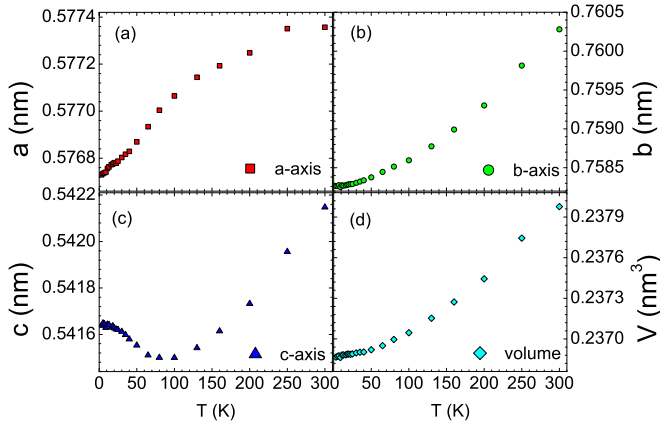
FIG. 2. The temperature evolution of the crystallographic parameters as determined by fitting the low-temperature XRPD data using the Le Bail method. Raw data used for the analysis are presented in Fig. SM2 [33].



FIG. 3. Temperature variation of the diffraction intensities as a function of $2\theta$ for NdMn$_{0.8}$Fe$_{0.2}$O$_3$. The color scale for the observed intensity is given to the right of the main plot of data collected on the E6 diffractometer at HZB.

In comparison, bulk probes found $T_N = 58.6(5)$ K [25]. A similar temperature evolution of the crystallographic parameters was observed in the case of the NdFeO$_3$ compound in the spin reorientation region [19], but in the case of NdMnO$_3$, the sudden drop of all three crystallographic parameters was observed at $T_N$ [10]. Therefore, the magnetoelastic coupling in NdMn$_{0.8}$Fe$_{0.2}$O$_3$ is different from NdMnO$_3$, but it can be similar to NdFeO$_3$. No extra peaks were observed at temperatures below 300 K (see Fig. SM2 of Supplemental Material) [33], and there were no essential shifts of fractional coordinates (see Fig. SM3) [33], which would imply the presence of spin-rotation/octahedral-rocking that was detected in NdFeO$_3$ [17,18]. These results imply that no structural phase transitions exist in the temperature range $3 \leqslant T \leqslant 300$ K. Consequently, when determining the magnetic structure of NdMn$_{0.8}$Fe$_{0.2}$O$_3$ (see the next section), the crystal structure was fixed to be the orthorhombic structure, space group *Pnma*.

### B. Magnetic structure refinement

Although the XRPD study below 65 K suggests that the orthorhombic symmetry of the crystal structure remains unchanged, the NPD experiment revealed that intensities of some reflections increase with decreasing temperature, for example the (111) reflection, and a gradual increase of intensity appears, for example on the (010) reflection, which is forbidden by the space group *Pnma* [46] (Fig. 3). These changes are associated with magnetic ordering setting in below $T_N = 58.6(5)$ K, which is in agreement with our ac susceptibility and magnetization measurements [25]. Since all magnetic reflections can be indexed by integer *hkl* indices, the magnetic ordering wave vector is **k** = (000). Furthermore, below $T_1 \approx 13$ K, remarkable changes in the intensity of some magnetic peaks, namely the overlapping (121), (002), and (210) reflections and the (200) reflection, are observed; see Fig. 4. These increases of intensities indicate that the magnetic structure is evolving and/or the other magnetic ion is ordering. These low-temperature changes of the diffraction pattern onset at the temperature, $T_1 = 13$ K, where an anomaly is detected in the ac susceptibility [25]. For $T < T_1$, no additional magnetic
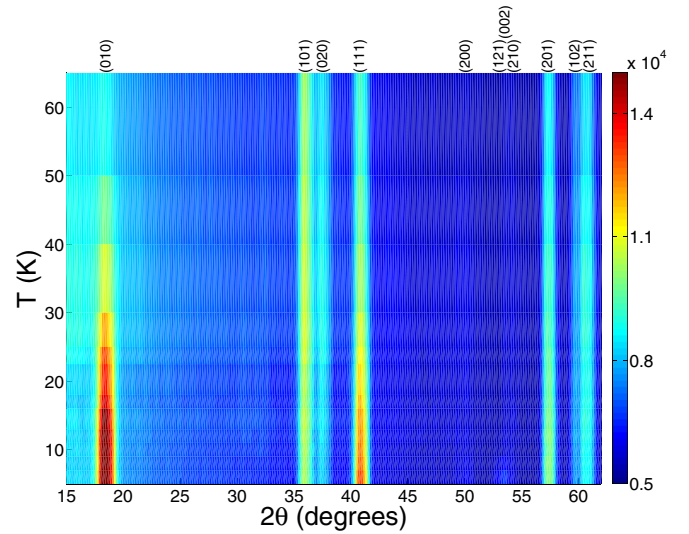
peaks appear, and the magnetic structure is described by the same propagation vector **k** = (000).

Assuming there is no spin-lattice-induced change in the space group, the possible magnetic modes compatible with the crystal symmetry have been obtained using the program BASIREPS [38]. For **k** = (000), the little group, $\Gamma_k$, coincides with the space group *Pnma*. Of the eight $\Gamma_i$'s for the *Pnma* 4*b* position of the Mn and Fe, four allow magnetic order such that

$$\Gamma_{\text{Mn/Fe}} = 3\left(\Gamma_1 + \Gamma_3 + \Gamma_5 + \Gamma_7\right). \quad (1)$$

For Nd atoms on the 4*c* site, the decomposition is

$$\Gamma_{\text{Nd}} = \Gamma_1 + \Gamma_4 + \Gamma_5 + \Gamma_8 + 2\left(\Gamma_2 + \Gamma_3 + \Gamma_6 + \Gamma_7\right). \quad (2)$$

The basis vectors obtained for each irreducible representation $\Gamma_i$ are reported in the Appendix; see Table III.

Based on the results for LaMnO$_3$ [47] and extrapolated generically to $R$MnO$_3$, it is widely accepted that the Mn sublattice orders at much higher temperatures than those at which the $R$ ions become polarized due to the $R$-Mn interaction. However, several different magnetic structures for NdMnO$_3$ have been reported by various groups, including the possibility that Nd ions order already at $T_N$ [9,10,16,48]. For this reason, all possible magnetic structures allowed by the basic symmetry constraints were considered, including the independent ordering of Mn/Fe and Nd sublattices and the plausible case in which the Nd moments remain disordered (denoted as the $\Gamma_0$ state). In total, 36 model structures were compared with the NPD data sets collected at $T = 1.6$ K at HZB. When all experimentally detected peaks were described by a model structure and no extra peaks with intensities higher than the experimental noise were generated, then plausible matches were considered to be established between a model structure and the data. The next step involved Rietveld analysis starting with each plausible model structure. The results of this comprehensive analysis are summarized and tabulated in Table SM1 [33], where the magnetically ordered
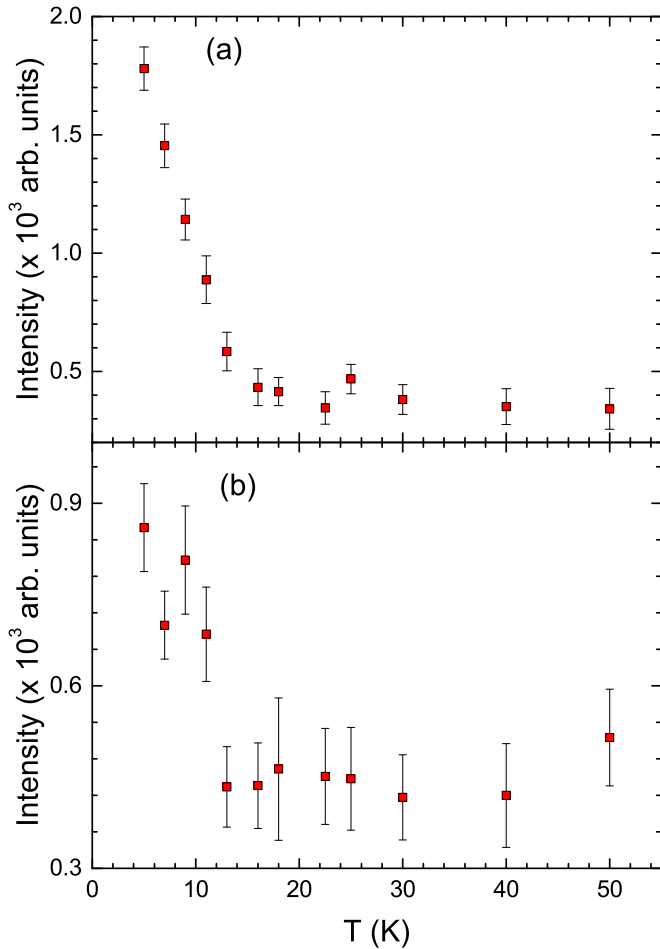
FIG. 4. Temperature variation of the integrated intensities of the (a) overlapping (121), (002), and (210) reflections, and (b) (200) reflection. Data collected on the E6 diffractometer at HZB.

state notation, $\Gamma_{i\text{Mn/Fe}}\Gamma_{j\text{Nd}}$, is defined and cross-referenced. This analysis resulted in four magnetic structures whose refined $R$-factors did not distinguish any single structure as the unambiguous solution. These four magnetic structures are as follows: $\Gamma_{5\text{Mn/Fe}}\Gamma_{7\text{Nd}}$, $\Gamma_{5\text{Mn/Fe}}\Gamma_{3\text{Nd}}$, $\Gamma_{5\text{Mn/Fe}}\Gamma_{5\text{Nd}}$, and $\Gamma_{5\text{Mn/Fe}}\Gamma_{0\text{Nd}}$.

In all cases, the best fit for $T = 1.6$ K is found to be $\Gamma_{5\text{Mn/Fe}}$ for the Mn/Fe sublattice, but the goodness-of-fit parameters cannot unambiguously distinguish between $\Gamma_{0\text{Nd}}$, $\Gamma_{3\text{Nd}}$, $\Gamma_{5\text{Nd}}$, and $\Gamma_{7\text{Nd}}$. The absence of any additional structural phase transitions in the XRPD suggests that the magnetic space group does not change at $T_1$. Also extrapolating from LaMnO$_3$ [47], it is generally accepted that the Mn sublattice orders at $T_N$. This inference implies that if the Nd sublattice orders, then it should order within the same magnetic space group as the Mn sublattice. Consequently, the $\Gamma_{3\text{Nd}}$ and $\Gamma_{7\text{Nd}}$ are not physically allowed, but $\Gamma_{0\text{Nd}}$ and $\Gamma_{5\text{Nd}}$ remain as plausible configurations. Note that the $\Gamma_{0\text{Nd}}$ notation means the Nd ions do not order into long-range magnetic structure, which is consistent with the statement that at $T_1$ the magnetic structure evolves, but no additional ion orders at that temperature. Therefore, the magnetic space group of NdMn$_{0.8}$Fe$_{0.2}$O$_3$ is assigned to be $Pn'ma'$.

Considering the $4b$ transition-metal site, the $\Gamma_5$ representation can host $A$-type (as for NdMnO$_3$) and $G$-type (as for NdFeO$_3$) antiferromagnetism. Since the $4b$ site hosts Mn and Fe ions, we have tried to fit independently the Mn and Fe magnetic moments. A second analysis was performed with Mn magnetic moments constrained to the $(A_x, F_y, 0)$ magnetic structure (as for NdMnO$_3$) and the Fe magnetic moments constrained to $(0, F_y, G_z)$ magnetic structure (as for NdFeO$_3$). Despite the fact that large seeds of initial fitting parameters were used (see Sec. II D), *all* fits in both cases converged to unphysical results. Consequently, these two options were rejected, leaving the only two possibilities that either the Mn or the Fe ions exclusively order. Since $T_N$ for $x = 0.2$ is smaller than for $x = 0$ and a minimum of $T_N$ is expected at concentrations $x \geqslant 0.25$ [25], one can expect that the Fe ions act only as a perturbation, and the magnetism is mainly driven by the Mn ions. As a result on the $4b$ site, only the Mn ions order and the possible magnetic ordering can be $\Gamma_{5\text{Mn}}\Gamma_{0\text{Nd}}$ or $\Gamma_{5\text{Mn}}\Gamma_{5\text{Nd}}$. Finally, the large seed initial fitting parameters test (see Sec. II D) for structures $\Gamma_{5\text{Mn}}\Gamma_{0\text{Nd}}$ and $\Gamma_{5\text{Mn}}\Gamma_{5\text{Nd}}$ revealed six local minima in the entire parameter space, where the fitting parameters resulted in physically meaningful values (see Table SM2 [33], where the numbering of the minima is also defined). From these six candidates, only two plausible descriptions emerge; see Table SM2 for details [33].

### C. Temperature dependences of the magnetic moments

The temperature dependences of the two remaining candidates for the magnetic structure are shown in Fig. 5. In the case of $\Gamma_{5\text{Mn}}\Gamma_{5\text{Nd}}$, the Nd ions order at $T_N$, but $\mu_{\text{Nd}y}$ exhibits an abrupt increase at $T_1$, and $\mu_{\text{Mn}y}$ flips to the opposite direction at the same temperature. In the case of $\Gamma_{5\text{Mn}}\Gamma_{0\text{Nd}}$, $T_1$ can be attributed to the evolution of the $\mu_{\text{Mn}y}$ component. In both cases, $T_1$ is also connected with the continuous decrease of the $\mu_{\text{Mn}z}$ component, which is typical for a spin-reorientation phase transition. Since this effect is rather weak, additional tests are needed to distinguish if the effect is real. The permitted reflections for the $G_z$ mode have constraints that $k$ is odd and $h + l = 2n + 1$. Consequently, the strongest contribution to the magnetic signal from the $G_z$ mode should be observed for the (110) reflection. Since the intensity of the (110) reflection is close to the background of NPD patterns collected at HZB, an additional NPD experiment focused on resolving this issue was performed at ORNL. The data from this experiment show unambiguously that the magnetic signal on the (110) reflection, Fig. 6, is stronger at 23(2) K than at 1.6(1) K, thereby confirming that the spin reorientation phase transition is a real effect.

According to a molecular field model [49], the temperature evolution of the total magnetic moment $\mu(T)$ follows a self-consistent expression written as

$$\mu(T) = \mu_0 B_J\left(\frac{3J}{(J+1)}\frac{\mu(T)}{\mu_0}\frac{T_N}{T}\right), \quad (3)$$

where $\mu_0$ is the magnetic moment at $T = 0$, $B_J$ is the Brillouin function, and $T_N$ is the ordering temperature. Fits according to Eq. (3) yield $T_N = 58.7$ and 57.6 K for the $\Gamma_{5\text{Mn}}\Gamma_{5\text{Nd}}$ and $\Gamma_{5\text{Mn}}\Gamma_{0\text{Nd}}$ magnetic structures, respectively. The value
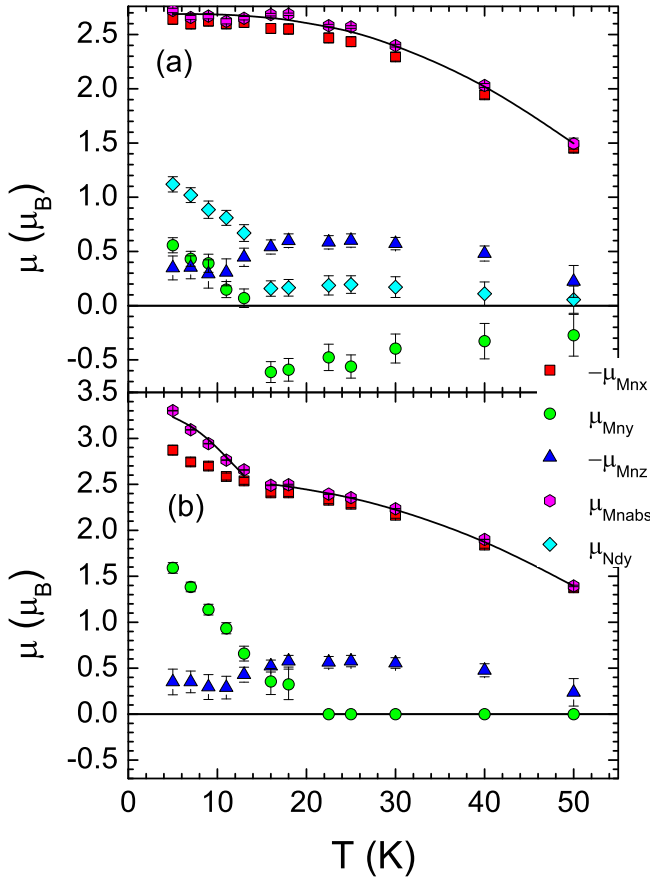
FIG. 5. The temperature evolution of the magnetic components and absolute value of the Mn magnetic moment for the magnetic structure (a) $\Gamma_{5Mn}\Gamma_{5Nd}$ and (b) $\Gamma_{5Mn}\Gamma_{0Nd}$. The solid lines represent the best fits according to Eq. (3).

of $T_N$ for the $\Gamma_{5Mn}\Gamma_{5Nd}$ magnetic structure is closer to $T_N = 58.6(5)$ K, obtained from bulk magnetization measurements [25]. The magnetic moment of the Mn sublattice extrapolated
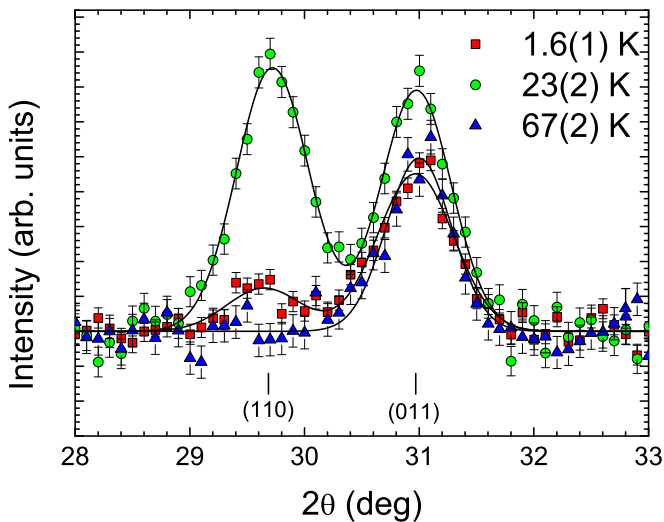


FIG. 6. The NPD patterns obtained, after subtracting a linear background, in the vicinity of the (110) and (011) reflections as measured on the HB-3 triple-axis instrument at ORNL. The lines represent Gaussian fits of the intensity.

to $T = 0$ K is 2.69 $\mu_B$ for $\Gamma_{5Mn}\Gamma_{5Nd}$, and this result is lower than $\mu_{Mn} = 3.87(3)$ $\mu_B$ reported for LaMnO$_3$ [47]. On the other hand, for the $\Gamma_{5Mn}\Gamma_{0Nd}$ structure, the magnetic moment in the $T \rightarrow 0$ limit is $\mu_{Mn} = 3.27$ $\mu_B$, which is much closer to $\mu_{Mn}$ reported for LaMnO$_3$ [47]. However, the data for the $\Gamma_{5Mn}\Gamma_{0Nd}$ structure are not well-modeled by a single Brillouin function, and this result may suggest the presence of a phase transition at $T_1$. Since specific-heat data of the NdMn$_{0.8}$Fe$_{0.2}$O$_3$ compound show no anomaly at $T_1$ [25], it is plausible that $T_1$ is not connected with a phase transition. Additionally, the $R$-factors determined at 20 K are much lower for the $\Gamma_{5Mn}\Gamma_{5Nd}$ magnetic structure than for the $\Gamma_{5Mn}\Gamma_{0Nd}$ structure (see Table SM3) [33]. Finally, a recent backscattering experiment [50] resolved a nonzero polarization of the Nd ions for $T < T_N$, so the $\Gamma_{5Mn}\Gamma_{0Nd}$ magnetic configuration can be eliminated as a physical option, thereby leaving $\Gamma_{5Mn}\Gamma_{5Nd}$ as the only possible description. Specifically, the magnetic configuration is $(A_x, F_y, G_z)$ for Mn ions and $(0, f_y, 0)$ for the Nd sublattice in the whole temperature range 1.6 K $\leqslant T \leqslant T_N$.

## IV. NdMnO$_3$ MAGNETIC STRUCTURE BY DENSITY FUNCTIONAL THEORY CALCULATIONS

In the previous section, the magnetic structure of NdMn$_{0.8}$Fe$_{0.2}$O$_3$ was experimentally established to be $Pn'ma'$ $(A_x, F_y, G_z) + (0, f_y, 0)$. Since our analysis of NdMn$_{0.8}$Fe$_{0.2}$O$_3$ resulted in a magnetic structure that is different from the most accepted magnetic structure of the NdMnO$_3$ phase, but there have been some inconsistencies in the literature about the NdMnO$_3$ magnetic structure [9,10,16,48], this section describes a theoretical approach to understand the magnetic structure of pure NdMnO$_3$.

To start, varying $U$ and $J$ values as initial parameters yielded $U_{Nd} = 5$ eV, $J_{Nd} = 0.1$ eV for the $f$-shell of Nd, and with $U_{Mn} = 10$ eV and $J_{Mn} = 2$ eV for the $d$-shell of Mn atoms to preserve the insulating behavior and the magnetic moment length. These calculations ultimately led to values for the magnetic moments $\mu_{Nd} = 1.4$ $\mu_B$ and $\mu_{Mn} = 3.9$ $\mu_B$ and to a band gap of 1.75 eV, and these results are comparable to experimental observations [9,10,25,51]. These first-principles calculations revealed that the total magnetic moment of the Nd atom is reduced by the large orbital moment $\sim 1.5$ $\mu_B$/atom that is antiparallel with respect to its spin moment of 2.9 $\mu_B$/atom.

Next, the crystallographic structure was optimized by performing a complete relaxation of the lattice vectors as well as the atomic positions and internal degrees of freedom. During this initial optimization, two different types of exchange interactions, either antiferromagnetic or ferromagnetic between Mn spins, were considered. This crystallographic optimization led, in both cases, to a decrease of the space-group symmetry from $Pnma$ to $P2_1/c$. However, a closer look at the optimized structure revealed, in both cases, only minor shifts of the $y$-position of the Nd ion, from 1/4 to $0.250\epsilon$, where $\epsilon$ stands for a nonzero digit lower than 5, but such small shifts are below the precision of the experimental methods. Consequently, orthorhombic symmetry (space group $Pnma$) was employed in all of the following steps of the calculations.

Ultimately, two different crystallographic structures were obtained, and for the purposes of these numerical studies,

TABLE II. The total energy differences in meV per atom with respect to the ground state of $NdMnO_3$ for the four plausible magnetically ordered states ($\Gamma_{iMn}\Gamma_{jNd}$; see Tables III and SM1 [33] for definitions of the states) and for the $p_{AF}$ (antiferromagnetic Mn-Mn), $p_F$ (ferromagnetic Mn-Mn), and $p_{exp}$ (experimental) lattice structures; see text for details.

| Magnetic state | Mn | Nd | $p_{AF}$ | $p_F$ | $p_{exp}$ |
|---|---|---|---|---|---|
| $\Gamma_{5Mn}\Gamma_{7Nd}$ | $(A_x, F_y, G_z)$ | $(f_x, 0, 0)$ | 10.2 | 12.5 | 9.5 |
| $\Gamma_{5Mn}\Gamma_{3Nd}$ | $(A_x, F_y, G_z)$ | $(0, 0, f_z)$ | 25.5 | 41.2 | 10.7 |
| $\Gamma_{5Mn}\Gamma_{5Nd}$ | $(A_x, F_y, 0)$ | $(0, f_y, 0)$ | 23.5 | 0.0 | 0.0 |
| $\Gamma_{5Mn}\Gamma_{0Nd}$ | $(A_x, F_y, G_z)$ | disordered | 0.0 | 1.0 | 2.4 |

these structures are denoted as $p_{AF}$ and $p_F$. When assuming antiferromagnetic interactions between the Mn ions, the $p_{AF}$ state is identified with lattice parameters $a = 0.5968$ nm, $b = 0.7702$ nm, and $c = 0.5500$ nm. Conversely, when assuming ferromagnetic interactions between the Mn ions, the $p_F$ configuration is found with lattice parameters $a = 0.5987$ nm, $b = 0.7659$ nm, and $c = 0.5505$ nm. Both structures were obtained by relaxing all degrees of freedom, while only the initial magnetic pattern was different. The optimized lattice parameters are roughly 1.5–2.5 % higher than the experimentally determined lattice parameters as presented in Sec. III A and Table I, and $p_{exp}$ will designate the observed lattice. These results are consistent with the well-known over-binding effects of the GGA (PBE) exchange-correlation approximation employed for this work; see Sec. II E for details. Furthermore, such small differences in lattice parameters indicate a very good match between theory and experiment.

Finally, four magnetically ordered states, namely $\Gamma_{5Mn}\Gamma_{7Nd}$ [Mn $(A_x, F_y, G_z)$ and Nd $(f_x, 0, 0)$], $\Gamma_{5Mn}\Gamma_{3Nd}$ [Mn $(A_x, F_y, G_z)$ and Nd $(0, 0, f_z)$], $\Gamma_{5Mn}\Gamma_{5Nd}$ [Mn $(A_x, F_y, 0)$ and Nd $(0, f_y, 0)$], and $\Gamma_{5Mn}\Gamma_{0Nd}$ [Mn $(A_x, F_y, G_z)$ and with Nd disordered] were introduced for $p_{AF}$, $p_F$, and $p_{exp}$ structures, and only the electronic degrees of freedom were converged, i.e., the atomic positions were kept fixed.

The calculated total energies for each crystallographic structure—$p_{AF}$, $p_F$, and $p_{exp}$—and the plausible magnetically ordered states are summarized in Table II. From this tabulation, one immediately notices that the total energies of all three structures $p_{AF}$, $p_F$, and $p_{exp}$ with magnetic ordering of $\Gamma_{5Mn}\Gamma_{7Nd}$ and $\Gamma_{5Mn}\Gamma_{3Nd}$ are higher in energy than two other structures ($\Gamma_{5Mn}\Gamma_{5Nd}$ and $\Gamma_{5Mn}\Gamma_{0Nd}$), with the exception of $p_{AF}$ and $\Gamma_{5Mn}\Gamma_{5Nd}$. Consequently, these higher-energy results are excluded from further consideration.

At this point, magnetically ordered options remain, $\Gamma_{5Mn}\Gamma_{5Nd}$ and $\Gamma_{5Mn}\Gamma_{0Nd}$, which have very similar total energies for a fixed geometry to those in experimental studies ($p_{exp}$ structure) and for the ferromagnetically ordered Mn-Mn option $p_F$. However, the last row in Table II, with the magnetically ordered state $\Gamma_{5Mn}\Gamma_{0Nd}$, requires special attention since a "randomly" oriented $\mu_{Nd} = 1.4 \mu_B$/atom was used. To improve the "randomness," the simulation window was increased by a factor of 2 in every dimension to give a $2 \times 2 \times 2$ supercell containing 160 atoms, of which 16 are Nd atoms. (Periodic boundary conditions means that only magnetic moments inside the supercell are really random.)

This supercell approach did not change any of the details of the calculation (e.g., stability and magnetic ordering of the Mn atoms), and now the average Nd magnetic moment was closer to zero, as the statistics were significantly improved. Therefore, these calculations cannot unambiguously determine if Nd ions order or not, leaving both of these possibilities acceptable from a theoretical point of view.

## V. DISCUSSION

The $NdMn_{0.8}Fe_{0.2}O_3$ compound mixes an orthomanganite and orthoferrite with similar structures, except for the Jahn-Teller long bond of the Mn. Magnetically, $NdMnO_3$ is highly anisotropic with $A$-type antiferromagnetism [9,10] and $NdFeO_3$ is weakly anisotropic with $G$-type antiferromagnetism [17,18]. Our study is an investigation of single-ion doping in the anisotropic-$A$-type, pseudo-isotropic-$G$-type phase diagram to better understand the experimental magnetic structure.

The magnetic structure of $NdMn_{0.8}Fe_{0.2}O_3$ was unambiguously identified to be $\Gamma_5$ $(A_x, F_y, G_z)$ for the Mn ions over the whole temperature range 1.6 K $\leqslant T \leqslant T_N$. This structure is within the magnetic space group of $NdMnO_3$ and the high-temperature magnetic structure of $NdFeO_3$. On the other hand, in the low-temperature magnetic structure of $NdFeO_3$, $G$-type antiferromagnetism is accommodated by the $y$ direction, which means the $\Gamma_3$ representation. The most surprising finding of this work is that the magnetic structure of the Nd sublattice is also within the $\Gamma_5$ $(0, f_y, 0)$ representation, and the Nd ions exhibit long-range magnetic order at temperatures below $T_N$. This finding is different from $NdMnO_3$, where the ordering of Nd ions was reported only below $T_1 \approx 20$ K [10] and was different also from $NdFeO_3$, where the ordering of the Nd sublattice is suppressed below 4.5 K [20]. On the other hand, Chatterji *et al.* [15] conclude from their neutron backscattering data that the "finite energy of the inelastic peak and its much smaller temperature dependence at $T > 20$ K (are) due to the polarization of the Nd magnetic moment by the field of Mn moments." In fact, the finite energy of the inelastic peak in $NdMnO_3$ was observed below 40 K. A similar effect was also observed by our neutron backscattering experiment performed on $NdMn_{0.8}Fe_{0.2}O_3$ below $T_N$ [50]. The backscattering results prove the Nd ions become polarized at $T_N$. Since the backscattering experiment probes events with a characteristic time scale $\sim 10^{-9}$ s, this experiment cannot distinguish polarized Nd ions in short-range magnetic correlations from those in static long-range magnetic structure. Consequently, the Nd ions order at $\approx 20$ K in the case of $NdMnO_3$ [10,15], whereas the Nd ions order at $T_N$ in $NdMn_{0.8}Fe_{0.2}O_3$, even though both compounds exhibit essentially the same neutron backscattering spectra.

Our analysis shows that the effect observed at $T_1 \approx 13$ K by ac susceptibility is the spin reorientation effect. Such an effect was not observed in $NdMnO_3$, but spin reorientation is well reported for the $NdFeO_3$ compound [19]. Presumably, the Fe ions start to destabilize the magnetic structure of the Mn sublattice at the concentration studied in this work ($x = 0.2$), and the spin reorientation is a consequence of Fe doping. Another consequence is the stabilization of the long-range magnetic structure of Nd ions.

Finally, in all of the diffraction data sets, there is one sharp reflection for a given family of planes. However, as the crystal and magnetic structures of the parent compounds are so similar, it is possible that minor chemical inhomogeneities exist over nanometer-sized length scales [52]. Along with subtleties of stoichiometry, such effects may be important when comparing samples from different laboratories.

## VI. CONCLUSIONS

The magnetic structure of $NdMn_{0.8}Fe_{0.2}O_3$ has been investigated using NPD. The resulting model for $T < T_N$ has wave vector $\mathbf{k} = (000)$ and the $\Gamma_5$ magnetic structure with the $(A_x, F_y, G_z)$ configuration for the Mn ions and the $(0, f_y, 0)$ arrangement for the Nd ions. The magnetic structure follows the dominant Mn ion, but it finds a way to accommodate the interactions of the less populous Fe ion, which affects the fine details of the magnetic structure. Quantitative analyses to substantiate this model are underway with additional probes.

## ACKNOWLEDGMENTS

## APPENDIX

In Table III, we present the basis vectors obtained for each irreducible representation $\Gamma_i$.

TABLE III. Basis vectors for space group $Pnma$ (No. 62 in International Tables for Crystallography [46]) and $\mathbf{k} = (000)$. Atomic positions for Mn: Mn1 $(0,0,\frac{1}{2})$, Mn2 $(\frac{1}{2},0,0)$, Mn3 $(0,\frac{1}{2},\frac{1}{2})$, Mn4 $(\frac{1}{2},\frac{1}{2},0)$; and for Nd: Nd1 $(x,\frac{1}{4},z)$, Nd2 $(-x + \frac{1}{2},\frac{3}{4},z + \frac{1}{2})$, Nd3 $(-x,\frac{3}{4},-z)$, Nd4 $(x + \frac{1}{2},-y + \frac{1}{2},-z + \frac{1}{2})$.

|  | Mn($4b$) | Nd($4c$) |
|---|---|---|
| $\Gamma_1$ | $(G_x, C_y, A_z)$ | $(-, c_y, -)$ |
| $\Gamma_2$ |  | $(g_x, -, a_z)$ |
| $\Gamma_3$ | $(C_x, G_y, F_z)$ | $(c_x, -, f_z)$ |
| $\Gamma_4$ |  | $(-, g_y, -)$ |
| $\Gamma_5$ | $(A_x, F_y, G_z)$ | $(-, f_y, -)$ |
| $\Gamma_6$ |  | $(a_x, -, g_z)$ |
| $\Gamma_7$ | $(F_x, A_y, C_z)$ | $(f_x, -, c_z)$ |
| $\Gamma_8$ |  | $(-, a_y, -)$ |
| $F = m_1 + m_2 + m_3 + m_4$ | $C = m_1 - m_2 + m_3 - m_4$ | |
| $G = m_1 - m_2 - m_3 + m_4$ | $A = m_1 + m_2 - m_3 - m_4$ | |

[1] L. Martin and R. Ramesh, Acta Mater. **60**, 2449 (2012).

[2] J. M. D. Coey, Philos. Trans. R. Soc. London, Ser. A **356**, 1519 (1998).

[3] M. B. Salamon and M. Jaime, Rev. Mod. Phys. **73**, 583 (2001).

[4] A. P. Ramirez, J. Phys.: Condens. Matter **9**, 8171 (1997).

[5] F. Millange, S. de Brion, and G. Chouteau, Phys. Rev. B **62**, 5619 (2000).

[6] A. Glavic, H. Dixit, V. R. Cooper, and A. A. Aczel, Phys. Rev. B **93**, 140413 (2016).

[7] R. L. Carlin, *Magnetochemistry* (Springer-Verlag, Berlin, 1986).

[8] J. Bartolomé, E. Palacios, M. D. Kuz'min, F. Bartolomé, I. Sosnowska, R. Przeniosło, R. Sonntag, and M. M. Lukina, Phys. Rev. B **55**, 11432 (1997).

[9] A. Muñoz, J. A. Alonso, M. J. Martínez-Lope, J. L. García-Muñoz, and M. T. Fernández-Díaz, J. Phys.: Condens. Matter **12**, 1361 (2000).

[10] T. Chatterji, B. Ouladdiaf, and D. Bhattacharya, J. Phys.: Condens. Matter **21**, 306001 (2009).

[11] H. A. Jahn and E. Teller, Proc. R. Soc. London, Ser. A **161**, 220 (1937).

[12] V. Skumryev, F. Ott, J. M. D. Coey, A. Anane, J.-P. Renard, L. Pinsard-Gaudart, and A. Revcolevschi, Eur. Phys. J. B **11**, 401 (1999).

[13] Z. Jirák, J. Hejtmánek, E. Pollert, M. Maryško, and M. Dlouhá, J. Appl. Phys. **81**, 5790 (1997).

[14] D. O'Flynn, C. V. Tomy, M. R. Lees, A. Daoud-Aladine, and G. Balakrishnan, Phys. Rev. B **83**, 174426 (2011).

[15] T. Chatterji, G. J. Schneider, L. van Eijck, B. Frick, and D. Bhattacharya, J. Phys.: Condens. Matter **21**, 126003 (2009).

[16] F. Bartolomé, J. Herrero-Albillos, L. M. García, J. Bartolomé, N. Jaouen, and A. Rogalev, J. Appl. Phys. **97**, 10A503 (2005).

[17] K. P. Belov, M. A. Belyanchikova, A. M. Kadomtseva, I. B. Krynetskii, T. M. Ledneva, T. L. Ovchinnikova, and V. A. Timofeeva, Fiz. Tverd. Tela **14**, 248 (1972) [Sov. Phys. Solid State **14**, 199 (1972)].

[18] N. Koshizuka and K. Hayashi, J. Phys. Soc. Jpn. **57**, 4418 (1988).

[19] W. Sławiński, R. Przeniosło, I. Sosnowska, and E. Suard, J. Phys.: Condens. Matter **17**, 4605 (2005).

[20] R. Przeniosło, I. Sosnowska, and B. Frick, J. Magn. Magn. Mater. **305**, 186 (2006).

[21] I. Troyanchuk, M. Bushinsky, H. Szymczak, M. Baran, and K. Bärner, J. Magn. Magn. Mater. **312**, 470 (2007).

[22] F. K. Chiang, M. W. Chu, F. C. Chou, H. T. Jeng, H. S. Sheu, F. R. Chen, and C. H. Chen, Phys. Rev. B **83**, 245105 (2011).

[23] M. Mihalik, Z. Jagličcić, M. Fitta, V. Kavečanský, K. Csach, A. Budziak, J. Briančin, M. Zentková, and M. Mihalik, J. Alloys Compd. **687**, 652 (2016).

[24] M. Mihalik Jr., M. Mihalik, Z. Jagličcić, R. Vilarinho, J. Agnostinho Moreira, E. Queiros, P. B. Tavares, A. Almeida, and M. Zentková, Physica B **506**, 163 (2017).

[25] M. Mihalik, M. Mihalik, M. Fitta, M. Bałanda, M. Vavra, S. Gabáni, M. Zentková, and J. Briančin, J. Magn. Magn. Mater. **345**, 125 (2013).

[26] M. Mihalik, S. Matas, M. Vavra, J. Briančin, M. Mihalik, M. Fitta, V. Kavečanský, and J. Kopeček, J. Cryst. Growth **401**, 605 (2014).

[27] J. Lazurova, M. Mihalik, M. Mihalik Jr., M. Vavra, M. Zentkova, J. Briancin, M. Perovic, V. Kusigerski, O. Schneeweiss, P. Roupcova, K. V. Kamenev, M. Misek, and Z. Jaglicic, J. Phys.: Conf. Ser. **592**, 012117 (2015).

[28] I. Troyanchuk, J. Magn. Magn. Mater. **231**, 53 (2001).

[29] T. Tawaraya, K. Katsumata, and H. Yoshizawa, J. Phys. Soc. Jpn. **49**, 1299 (1980).

[30] L. Bevaart, E. Frikkee, J. Lebesque, and L. de Jongh, Solid State Commun. **25**, 539 (1978).

[31] E. Torikai, A. Ito, Y. Takeda, K. Nagamine, K. Nishiyama, Y. Syono, and H. Takei, Solid State Commun. **58**, 839 (1986).

[32] R. Mahendiran, A. Maignan, C. Martin, M. Hervieu, and B. Raveau, Phys. Rev. B **62**, 11644 (2000).

[33] See Supplemental Material at http://link.aps.org/supplemental/ 10.1103/PhysRevB.96.134430 for additional projections of the magnetic structures, the temperature variation of the XRPD data, the temperature dependences of the fitted fractional coordinates of Nd and O, a tabulation of plausible magnetic structures, and the magnetic moment sizes resolved from NPD data at 2 and 20 K.

[34] K. Momma and F. Izumi, J. Appl. Crystallogr. **44**, 1272 (2011).

[35] O. Pena, M. Bahout, K. Ghanimi, P. Duran, D. Gutierrez, and C. Moure, J. Mater. Chem. **12**, 2480 (2002).

[36] D. Kriegner, Z. Matěj, R. Kužel, and V. Holý, J. Appl. Crystallogr. **48**, 613 (2015).

[37] J. Rodríguez-Carvajal, Physica B **192**, 55 (1993).

[38] FullProf-Team, FullProf Suite (2016), version of February 2016, http://www.ill.eu/sites/fullprof.

[39] P. Hohenberg and W. Kohn, Phys. Rev. **136**, B864 (1964).

[40] G. Kresse and J. Furthmüller, Phys. Rev. B **54**, 11169 (1996).

[41] G. Kresse and J. Furthmüller, Comput. Mater. Sci. **6**, 15 (1996).

[42] J. P. Perdew, K. Burke, and M. Ernzerhof, Phys. Rev. Lett. **77**, 3865 (1996).

[43] H. J. Monkhorst and J. D. Pack, Phys. Rev. B **13**, 5188 (1976).

[44] S. L. Dudarev, G. A. Botton, S. Y. Savrasov, C. J. Humphreys, and A. P. Sutton, Phys. Rev. B **57**, 1505 (1998).

[45] V. Cherepanov, L. Barkhatova, A. Petrov, and V. Voronin, J. Solid State Chem. **118**, 53 (1995).

[46] T. Hahn (ed.), *International Tables for Crystallography, Volume A, Space Group Symmetry*, 5th ed. (Wiley, 2005).

[47] F. Moussa, M. Hennion, J. Rodriguez-Carvajal, H. Moudden, L. Pinsard, and A. Revcolevschi, Phys. Rev. B **54**, 15149 (1996).

[48] S. Jandl, S. Barilo, S. Shiryaev, A. Mukhin, V. Ivanov, and A. Balbashov, J. Magn. Magn. Mater. **264**, 36 (2003).

[49] D. P. Kozlenko, I. N. Goncharenko, B. N. Savenko, and V. I. Voronin, J. Phys.: Condens. Matter **16**, 6755 (2004).

[50] D. M. Pajerowski *et al.* (unpublished).

[51] R. Shetkar and A. Salker, J. Mater. Sci. Technol. **26**, 1098 (2010).

[52] D. Shulyatev, N. Kozlovskaya, A. Pestun, Y. Mukovskii, L. Elochina, and R. Zainullina, J. Cryst. Growth **311**, 4142 (2009).